

Simulations of the cosmic infrared and submillimeter background for future large surveys

I. Presentation and first application to Herschel/SPIRE and Planck/HFI

N. Fernandez-Conde, G. Lagache, J.-L. Puget, and H. Dole

Institut d’Astrophysique Spatiale (IAS), bâtiment 121, Université Paris-Sud 11 and CNRS (UMR 8617), 91405 Orsay, France
e-mail: [nestor.fernandez; guilaine.lagache; jean-loup.puget; herve.dole]@ias.u-psud.fr

Received 29 June 2007 / Accepted 2 October 2007

ABSTRACT

Context. The coming Planck and Herschel missions will survey the sky at unprecedented angular scales and sensitivities. Simulations are needed for better interpreting the results of the surveys and for testing new methods of, e.g., source extraction and component separation.

Aims. We present new simulations of the infrared and submillimeter cosmic background, including the correlation between infrared galaxies. The simulations were used to quantify the source-detection thresholds for Herschel/SPIRE and Planck/HFI, as well as to study the detectability of the cosmic infrared background correlated fluctuations.

Methods. The simulations are based on an empirical model of IR galaxy evolution. For these correlations, we only included the linear clustering, assuming that infrared galaxies are biased tracers of the dark-matter fluctuation density field.

Results. We used the simulations with different bias parameters to predict the confusion noise for Herschel/SPIRE and Planck/HFI and the completeness levels. We also discuss the detectability of the linear clustering in Planck/HFI power spectra, including the foreground and backgrounds components.

Conclusions. Simulated maps and catalogs are publicly available online at <http://www.ias.u-psud.fr/irgalaxies/simulations.php>

Key words. infrared: galaxies – galaxies: evolution – cosmology: large-scale structure of Universe – methods: numerical

1. Introduction

The cosmic infrared background (CIB) ($\lambda \geq 8 \mu\text{m}$) is the relic emission of the formation and evolution of galaxies. The first observational evidence of this background was reported by Puget et al. (1996) and then confirmed by Hauser et al. (1998) and Fixsen et al. (1998). The discovery of a surprisingly high amount of energy in the CIB has shown the importance of studying its sources to understand how the bulk of stars was formed in the Universe. Deep cosmological surveys have been carried out thanks to ISO (see Genzel & Cesarsky 2000; Elbaz 2005, for reviews) mainly at $15 \mu\text{m}$ with ISOCAM (e.g. Elbaz et al. 2002); at 90 and $170 \mu\text{m}$ with ISOPHOT (e.g. Dole et al. 2001); to SPITZER at 24 , 70 , and $160 \mu\text{m}$ (e.g. Papovich et al. 2004; Dole et al. 2004) and to ground-based instruments such as SCUBA (e.g. Holland et al. 1998) and MAMBO (e.g. Bertoldi et al. 2000) at 850 and $1300 \mu\text{m}$, respectively. These surveys have allowed for a better understanding of the CIB and its sources (see Lagache et al. 2005, for a general review). Some of the results include: the energy of the CIB is dominated by starbursts although AGN (active galactic nucleus) contribute too, and the dominant contributors to the energy output are the LIRGs (luminous IR galaxies) at $z \sim 1$ and ULIRGs (ultra luminous IR galaxies) at $z \sim 2$ – 3 .

Determination of the CIB by the COBE satellite has been hindered by the accuracy of subtracting the foreground by only

providing just upper limits at 12 , 25 , and $60 \mu\text{m}$ (Hauser et al. 1998), lower limit has been derived at $24 \mu\text{m}$ by Papovich et al. (2004) as well as the contribution of $24 \mu\text{m}$ galaxies to the background at 70 and $160 \mu\text{m}$ (Dole et al. 2006). The contribution of the galaxies down to $60 \mu\text{Jy}$ at $24 \mu\text{m}$ is at least 79% of the $24 \mu\text{m}$ background, and 80% of the 70 and $160 \mu\text{m}$ background. For longer wavelengths, recent studies have investigated the contribution of populations selected in the near-IR to the far-infrared background (FIRB, $\lambda > 200 \mu\text{m}$): $3.6 \mu\text{m}$ selected sources to the $850 \mu\text{m}$ background (Wang et al. 2006) and $8 \mu\text{m}$ and $24 \mu\text{m}$ selected sources to the $850 \mu\text{m}$ and $450 \mu\text{m}$ backgrounds (Dye et al. 2006). Similar studies with Planck and Herschel will provide even more evidence of the nature of the FIRB sources.

Studying correlations in the spatial distribution of IR galaxies as a function of redshift is an essential observation (parallel to the studies of individual high-redshift, infrared, luminous galaxies), to understand the underlying scenario and physics of galaxy formation and evolution. A first study has been done using the $850 \mu\text{m}$ galaxies (Blain et al. 2004). Although the number of sources is quite small, they find evidence that submillimeter galaxies are linked to the formation of massive galaxies in dense environments destined to become rich clusters. This has now been directly supported by the detection of the clustering of high-redshift $24 \mu\text{m}$ selected ULIRGs and HyperLIRGs (Farrah et al. 2006; Magliocchetti et al. 2007). Studying correlations with individual IR galaxies is very hard due to either high

confusion noises, instrumental noises, or small fields of observation. It has been shown that the IR-background anisotropies could provide information on the correlation between the sources of the CIB and dark matter for large-scale structures (Knox et al. 2001; Haiman & Knox 2000, hereafter HK) and on the large-scale structure evolution. First studies at long wavelengths have only detected the shot-noise component of the fluctuations: Lagache & Puget (2000) at 170 μm , Matsuura et al. (2000) at 90 and 170 μm , Miville-Deschénes et al. (2001) at 60 and 100 μm . Lagache et al. (2007) and Grossan & Smoot (2007) report first detections of the correlated component using Spitzer/MIPS data at 160 μm . Lagache et al. (2007) measured a linear bias $b \sim 1.7$.

Future observations by Herschel and Planck will allow us to probe the clustering of IR and submm galaxies. Nevertheless these experiments will be limited, the confusion and instrumental noises will hinder detections of faint individual galaxies. Clustering thus has to be analysed in the background fluctuations (e.g. Negrello et al. 2007). The need for a prior understanding of what could be done by these experiments has motivated us to develop a set of realistic simulations of the IR and sub-mm sky.

In Sect. 2 we present the model on which are based our simulations. In Sect. 3 we discuss how the simulations are done and present a set of simulated sky maps and their corresponding catalogs. Different catalogs are created for 3 different levels of correlation between the IR galaxy emissivity and the dark-matter fluctuation density field (strong, medium, and no correlation). For each of these catalogs, we can create maps of the sky at any given IR wavelength and simulate how different instruments will see them. We focus in this paper on Planck/HFI and Herschel/SPIRE. In Sect. 4 we use the simulated maps to give predictions for the confusion noise, the completeness, and the detection limits for each of the study cases, including the instrumental noise. In Sect. 5 we present the power spectra of the CIB anisotropies for Planck/HFI and discuss their detectability against the significant sources of contamination (shot noise, cirrus, and cosmic microwave background (CMB)).

Throughout the paper the cosmological parameters were set to $h = 0.71$, $\Omega_\Lambda = 0.7$, $\Omega_m = 0.27$. For the dark-matter linear clustering we set the normalization to $\sigma_8 = 0.8$.

2. The model

2.1. Galaxies' empirical evolution model

The model of IR galaxies used for the simulations is from Lagache et al. (2003), revisited in Lagache et al. (2004) – hereafter the LDP model, see <http://www.ias.u-psud.fr/irgalaxies/model1.php>. This model is a flexible tool for planning surveys and developing analysis methods. The requirement was to build the simplest model of the luminosity function (LF) evolution with redshift, with the lowest number of parameters, but accounting for all statistical observational data between 5 μm and 1 mm. These are the spectral energy distribution of the CIB and its fluctuations, galaxy luminosity functions and their redshift evolution, as well as the existing source counts and redshift distributions.

The luminosity function of IR galaxies was modelled by a bimodal star-formation process: one associated with the passive phase of galaxy evolution (normal galaxies) and one associated with the starburst phase, mostly triggered by merging and interactions (starburst galaxies). Unlike for the starburst galaxies, the normal galaxy contribution to the luminosity function was considered mostly unchanged with redshift. The spectral energy

distribution (SED) changes with the luminosity of the source but is assumed constant with redshift for both populations in this simple model.

This model fits all the experimental data and has predicted that LIRGs ($10^{11} < L_{\text{IR}} < 10^{12}$) dominate at $z \approx 0.5$ –1.5 and that ULIRGs/HLIRGs ($L_{\text{IR}} > 10^{12}$) dominate at $z \approx 2$ –3 the energy distribution of the CIB. One example of the agreement between the model and the observations is shown in Fig. 2.

2.1.1. Number counts and CIB fluctuations

To illustrate the interest of studying the cosmic background fluctuations in the far-IR and submm domains, we use a simplistic approach for the number counts, following Lagache & Puget (2000). The source number counts can be schematically represented by a power law:

$$N(S > S_0) = N_0 \left(\frac{S}{S_0} \right)^{-\alpha} \quad (1)$$

where we set S_0 to be the detection limit for the sources and N_0 the number of sources with flux larger than S_0 .

In a Euclidean Universe with uniform density of the sources $\alpha = 1.5$. In the far-IR and submm, a steeper slope is observed with $\alpha = 2$ –3 in the regime where negative K -correction dominates. As an example, ISO observations found a slope of $\alpha = 2.2$ at 170 μm (Dole et al. 2001). Obviously, the number counts need to flatten for low fluxes to ensure that the CIB remains finite. For the rest of the discussion we will assume that $\alpha = 0$ for $S < S^*$. The total intensity of the CIB composed by all the sources up to S_{max} is given by:

$$I_{\text{CIB}} = \int_0^{S_{\text{max}}} S \frac{dN}{dS} dS.$$

For the Euclidean case the CIB intensity is dominated by sources near S^* .

Fluctuations from sources below the detection limit S_0 are given by

$$\sigma^2 = \int_0^{S_0} S^2 \frac{dN}{dS} dS.$$

Using $\frac{dN}{dS}$ given by Eq. (1) we get

$$\sigma^2 = \frac{\alpha}{2 - \alpha} N_0 S_0^2 \left[1 - \left(\frac{S^*}{S_0} \right)^{2-\alpha} \right].$$

For $\alpha > 2$ CIB fluctuations are dominated by sources close to S^* so that the same sources dominate both the FIRB and its fluctuations. Therefore by studying the fluctuations of the FIRB, we are also studying the sources that form the bulk of the contribution to the FIRB. We can check this conclusion with the number counts from the LDP model. Figure 3 shows that the same sources dominate the background and the fluctuations, but only for faint sources (for example $S_{850} \lesssim 50$ mJy). Therefore, it is necessary to subtract bright sources prior to any fluctuation analysis since they would otherwise dominate the fluctuations.

2.1.2. IR galaxy emissivity

For the purpose of the model we need to compute the mean IR galaxy emissivity per unit of comoving volume [$\text{W}/\text{Mpc}^3/\text{Hz}/\text{sr}$]. It is defined as

$$j_d(\nu, z) = (1+z) \int_{L_{\text{bol}}} L_{\nu'=\nu(1+z)} \frac{dN}{d\ln(L_{\text{bol}})} d\ln(L_{\text{bol}})$$

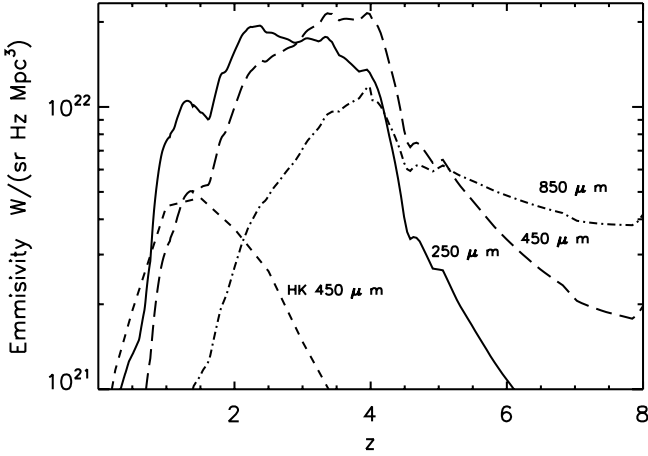


Fig. 1. Emissivities computed using the LDP model at (observed) 250 μm (continuous line), 450 μm (long-dashed line), and 850 μm (dotted-dashed line). The emissivity from HK at 450 μm (short-dashed line) is shown for comparison.

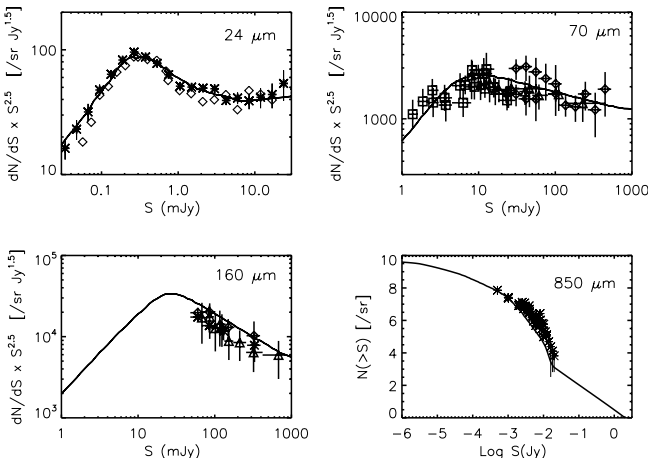


Fig. 2. Comparison of the observed source counts (data points) and model predictions (continuous lines). *Upper left:* 24 μm , *Upper right:* 70 μm , *Lower left:* 160 μm , *Lower right:* 850 μm .

where L is the luminosity (in W/Hz/sr), $\frac{dN}{d\ln(L_{\text{bol}})}$ is the comoving luminosity function (in Mpc $^{-3}$), and ν the observed frequency. We compute j_d using the SEDs and luminosity function from the LDP model which assumes that the SED depends only on L_{bol} . The resulting j_d is different from what is used by former approaches (HK, Knox et al. 2001). We can see the difference between the emissivity from our model and that of HK in Fig. 1. The crude model used for the emissivities by HK gives much lower emissivities than ours.

2.2. IR galaxy spatial distribution

Any model trying to account for CIB fluctuations must describe the statistical properties of the spatial distribution of the sources. The absence of a completely developed theoretical model for the distribution of the whole IR galaxy populations makes the empirical modelling of different distributions for the sources of the CIB necessary in order to prepare future observations. We used an empirical description for the spatial distribution of these sources, which has been used to create the simulated sky maps.

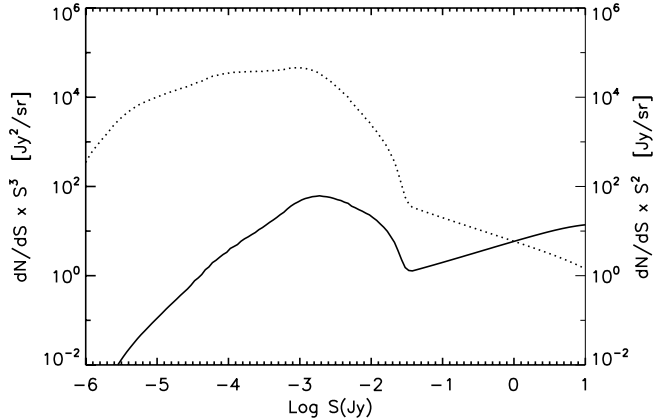


Fig. 3. Contributions of the sources of flux S (in Jy) per Log interval of S to the background (dotted line, right y axis) and fluctuations (continuous line, left y axis) at 850 μm .

The LDP model did not address the spatial distribution problem due to the lack of constraints at the time it was built. This is still mostly the case at the time of writing this work. The simulations by Dole et al. (2003) did not implement any correlation between IR galaxies and used an uncorrelated random distribution. However, since future experiments such as Herschel and Planck will be able to detect large-scale IR galaxy correlations ($\ell \lesssim 1000$), a model addressing this problem has become necessary. Herschel, with its high angular resolution, is expected to also probe correlations between galaxies in the same dark-matter haloes but in this study this correlation has not been considered for simplicity. We only consider the linear clustering i.e. IR galaxies as biased tracers of the dark matter haloes, with a linear relation between the dark-matter density-field fluctuations and IR emissivity.

We follow the prescription from Knox et al. (2001). The angular power spectrum that characterises the spatial distribution of the fluctuations of the CIB can be written as

$$C_l^v = \int \frac{dz dr}{r^2} a^2(z) j_d^2(\nu, z) b^2(k, \nu, z) P_M(k)|_{k=l/r} G^2(z). \quad (2)$$

In the equation several components can be identified, starting with a geometrical one $\frac{dz}{r^2} \frac{dr}{dz} a^2(z)$ (these terms take all the geometrical effects into account), followed by the galaxies emissivity $j_d(\nu, z)$ already described in Sect. 2.1.2, then the bias $b(k, \nu, z)$, and finally the power spectrum of dark-matter density fluctuations today $P_M(k)|_{k=l/r}$ and the linear theory growth function $G^2(z)$. Finally ℓ is the angular multipole, in the Limber approximation $k = l/r$, and r the proper motion distance. The way the power spectrum has been obtained is developed in the following subsections.

2.2.1. Dark-matter power spectrum

The power spectrum of the dark-matter distribution at $z = 0$ can be written as

$$P_M(k) \propto k T^2(k) \quad (3)$$

where $T(k, t)$ is the transfer function for a cold dark-matter universe (Bardeen et al. 1986). The linear theory growth function $G(z)$ writes as

$$G^2(z) = \frac{g^2(\Omega(z), \Omega_\Lambda(z))}{g^2(\Omega_0, \Omega_{\Lambda 0})(1+z)^2} \quad (4)$$

with

$$g[\Omega(z), \Omega_\Lambda(z)] = \frac{5}{2}\Omega(z) \times \left[\Omega(z)^{4/7} - \Omega_\Lambda(z) + \left(1 + \frac{1}{2}\Omega(z)\right) \left(1 + \frac{1}{70}\Omega_\Lambda(z)\right) \right]^{-1}.$$

$$\text{And } \Omega_\Lambda(z) = \frac{1 - \Omega_0}{\Omega_0(1 + z)^3 + 1 - \Omega_0}, \quad \Omega(z) = \frac{\Omega_0(1 + z)^3}{\Omega_0(1 + z)^3 + 1 - \Omega_0}.$$

2.2.2. Bias model

The bias of IR galaxies represents their level of correlation with the dark-matter density field. It can be expressed as a function of the spatial scale, the redshift, and the wavelength of observation. In this paper and due to lack of measurements for the bias, we consider a simplified constant bias b .

$$\frac{\delta j_d(k, \nu, z)}{\bar{j}_d(k, \nu, z)} = b \frac{\delta\rho(k, \nu, z)}{\bar{\rho}(k, \nu, z)}$$

where j_d is the emissivity of the IR galaxies per comoving unit volume, \bar{j}_d its mean level, and δj_d its fluctuations. Similarly, ρ is the dark matter density, $\bar{\rho}$ its mean value, and $\delta\rho$ is the linear-theory dark-matter density-field fluctuation.

We have better knowledge of the bias for optical and radio galaxies than for IR galaxies. Several studies have been able to measure the bias for the optical sources. As an example, a high bias ($b \sim 3$) has been found at $z \sim 3$ for the Lyman-Break Galaxies (Steidel et al. 1998; Giavalisco et al. 1998; Adelberger et al. 1998). It has been found as well that the bias increases with redshift both for the optical (Marinoni et al. 2006) and the radio (Brand et al. 2003) populations. The optical or radio bias could be misleading as a first guess for the bias of IR galaxies. IRAS has measured a low bias of IR galaxies at $z \sim 0$ (e.g. Saunders et al. 1992). Such a low bias is expected since the starburst activity in the massive dark-matter haloes in the local universe is very small. But we expect a higher IR bias at higher z , during the epoch of formation of galaxy clusters. Indeed, Lagache et al. (2007) report the first measurements of the bias, $b \sim 1.7$ in the CIB fluctuations at $160 \mu\text{m}$ using Spitzer data. The LDP model indicates that galaxies dominating the $160 \mu\text{m}$ anisotropies are at $z \sim 1$. This implies that infrared galaxies at high redshifts are biased tracers of mass, unlike in the local Universe. For an extensive review of the bias problem see Lahav & Suto (2004).

The IR bias could have very complex functional dependences, namely with the spatial frequency k , the redshift z , and the radiation frequency ν (for example if different populations of galaxies with different SEDs have different spatial distributions). However, for the simulations, simplified guesses for the bias were used, namely a constant bias of 1.5, 0.75, and 0.

Figures 4 show the angular power spectrum C_l for some Herschel and Planck wavelengths. The power spectra are shown for a constant bias $b = 1$. Since $C_l \propto b^2$, the predicted power spectrum scales as b^2 .

2.3. Discussion and implications of the model

The IR galaxy SED peaks near $80 \mu\text{m}$. This combines with the Doppler shift and causes observations at different wavelengths to probe different redshifts. Figure 5 shows the contributions to the power spectrum at $l = 1000$ for different redshifts, normalized to unity. The contributions to the same l come from higher redshift as wavelengths increase. The shorter wavelengths probe

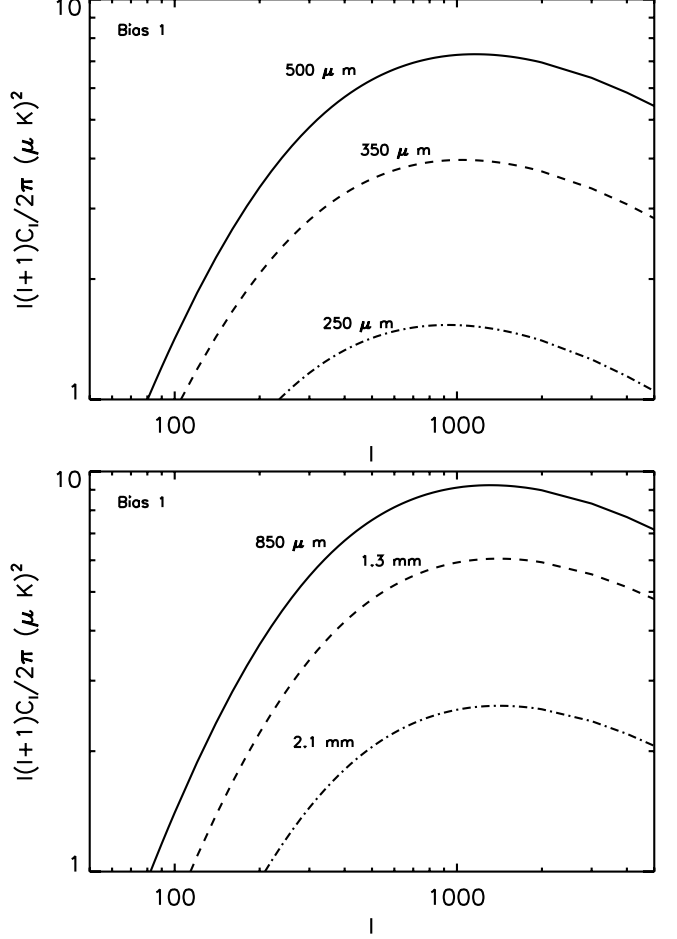


Fig. 4. Top: CIB Power spectrum with a bias $b = 1$ at Herschel/SPIRE wavelengths $500 \mu\text{m}$ (continuous line), $350 \mu\text{m}$ (dashed line), and $250 \mu\text{m}$ (dotted-dashed line). Bottom: CIB Power spectrum with a bias $b = 1$ at Planck/HFI CIB wavelengths $850 \mu\text{m}$ (continuous line), $1380 \mu\text{m}$ (dashed line), and $2097 \mu\text{m}$ (dotted-dashed line).

the lower redshifts because they are close to the maximum of the SED, while the longer wavelengths probe the higher redshifts due to the strong negative K -correction.

Figures 7 and 6 show the redshift contributions to the intensity of the CIB and to its integrated rms fluctuations for Planck/HFI and Herschel/SPIRE, assuming sources with $S > S_{\text{det}}$ have been removed – S_{det} corresponds to the source detection thresholds computed in Sect. 4.3. We see that the fluctuations and the FIRB are dominated by sources at the same redshift. Therefore, studying the fluctuations at different wavelengths will allow us to study the spatial distribution of the sources forming the FIRB at different redshifts.

The amount of fluctuations that come from sources at redshifts lower than 0.25 for the Planck/HFI case at $350 \mu\text{m}$ is noticeable from Fig. 7. This contrasts with the Herschel/SPIRE predictions where the bulk of the low- z sources contributing to the fluctuations in the Planck case are resolved. These individual detections with Herschel/SPIRE could allow their subtraction in the Planck maps. A similar approach could be used between the Herschel $500 \mu\text{m}$ and the Planck $550 \mu\text{m}$ channels, although it is more marginal. Using information on the fluctuations at shorter wavelengths to remove the low- z fluctuations from longer wavelength maps could be another approach to studying the fluctuations at high redshifts directly.

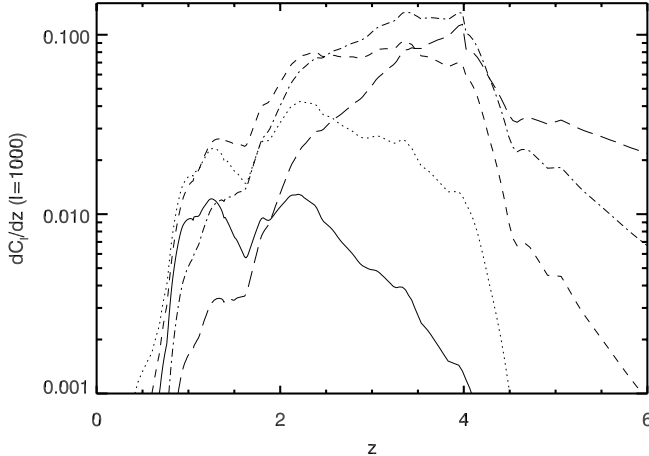


Fig. 5. Redshift contributions to the angular power spectrum $\frac{dC_l}{dz}$ at $l = 1000$ in μK^2 for different wavelengths: 250 μm (continuous line), 350 μm (dotted line), 550 μm (dashed line), 850 μm (dotted-dashed line), and 1380 μm (long dashed line).

A similar model has been developed by HK and revisited by Knox et al. (2001). We compare the HK and our C_1 prediction at 850 μm in Fig. 8 (for the comparison, the same bias and σ_8 is used). Our model is 2 times higher mainly due to our higher prediction for the IR galaxy emissivity. Similar results are found for other wavelengths.

3. The simulations

The simulations were computed by an IDL program that calculates the dark-matter power spectrum and spreads the galaxies in the map according to their correlation with the dark-matter density field. The CIB power spectrum is calculated as explained in Sect. 2.

To create the maps, two assumptions were made: first that all the galaxies share the same spatial distribution independently of their luminosities; second that both IR and normal galaxies share the same spatial distribution. This second assumption was made to avoid too many free parameters in the simulations, the contributions of both populations being well separated in redshift this assumption is a weak one.

The process for the creation of a virtual catalog can be summarised as follows. For a given wavelength, we create the map as a superposition of maps at different redshifts from $z = 0$ to $z = 6$. The separation in redshift slices decorrelates the emission from very distant regions of the modelled volume of the universe. In order to do so, we divided the maps in slices covering $dz = 0.1$. We can see the size of these slices for different redshifts in Table 1. For all redshift ranges the size of the slices is bigger than the measured comoving correlation lengths (for all populations of galaxies). We then construct a brightness map for each redshift slice by adding: 1) a constant map with the mean surface brightness predicted by the LDP model for that z slice, 2) a map of the fluctuations for the given bias predicted by our spatial distribution model for that z slice. The fluctuations are not correlated between z slices. The brightness map is then converted into flux map. At each luminosity, this can be converted into maps of numbers of sources. These numbers of sources are then redistributed into smaller z slices (inside the 0.1 slice) to refine the luminosity/flux relation. Note that all sources have the same underlying low frequency spatial distribution (but not the same positions) per $dz = 0.1$ slice. The position, luminosity, type (normal or starburst) and redshift of all sources are stored in a

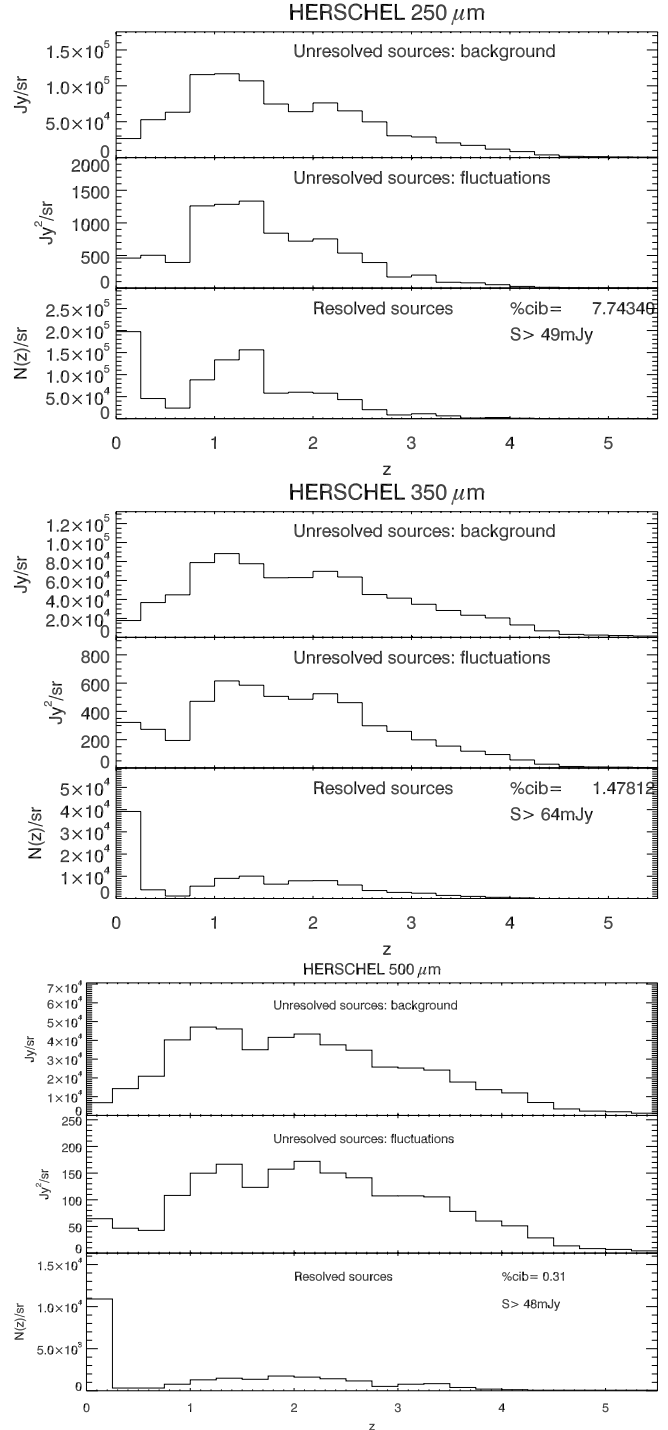


Fig. 6. Redshift contribution to the FIRB (top panels) and its fluctuations (middle panels). Also shown are the redshift distributions of the detected sources (bottom panels) for a typical large Herschel/SPIRE deep survey (see Sect. 4.3). From top to bottom: 250 μm , 350 μm and 500 μm .

catalog. Since we know these four parameters for all the sources, we can now create maps of the sky at any given wavelength. To simulate the observations, the map is convolved with the point spread function (PSF) of the chosen instrument.

For the purpose of this paper we have created Planck/HFI maps at 350, 550, 850, 1380 and 2097 microns and Herschel/SPIRE maps at 250, 350 and 500 microns. A description of the wavelengths and spatial resolution of the maps

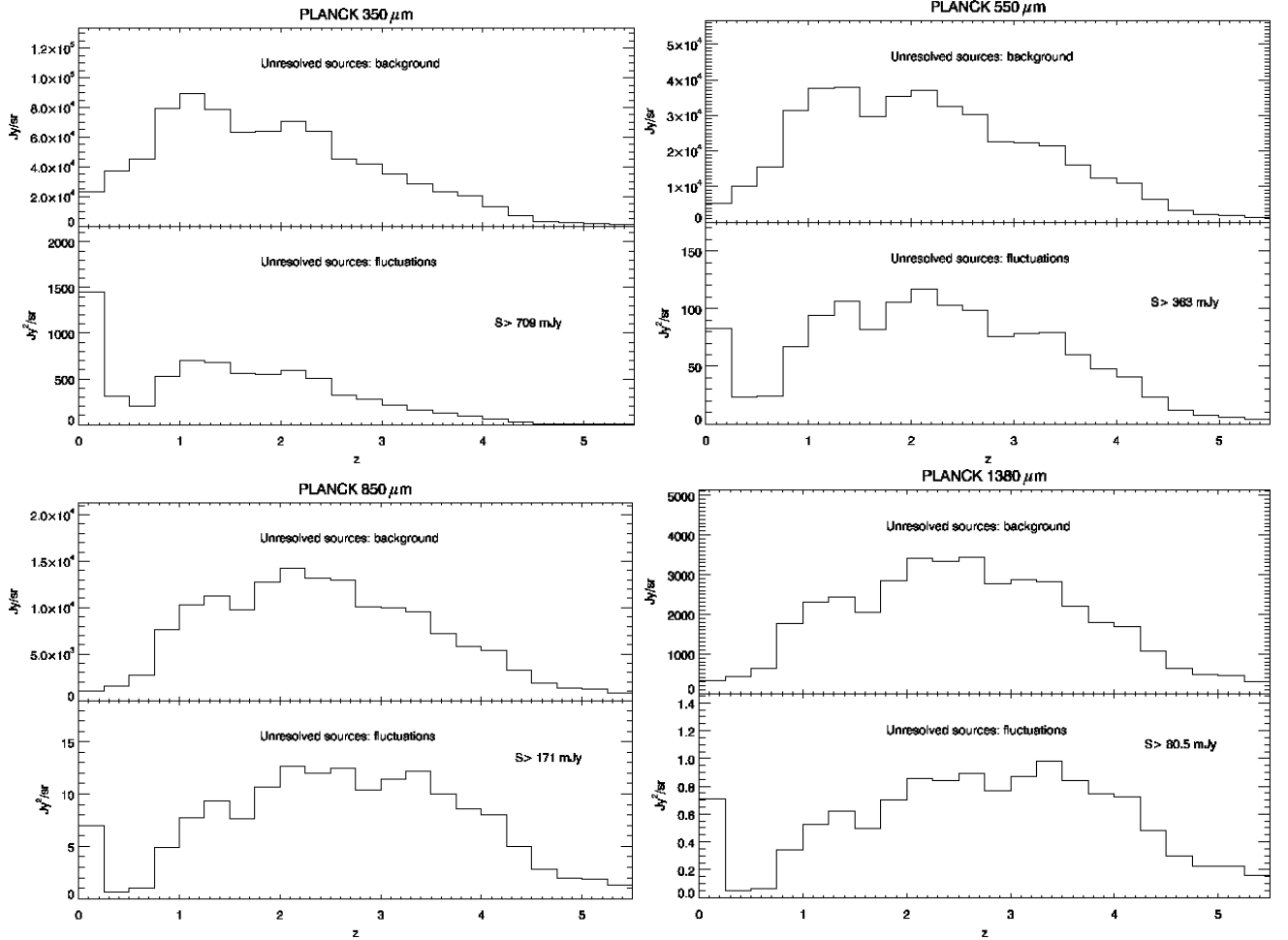


Fig. 7. Redshift contribution to the FIRB (*top panels*) and its fluctuations (*bottom panels*) for a Planck simulation ($dz = 0.25$) at $350\,\mu\text{m}$ (*top-left figure*), $550\,\mu\text{m}$ (*top-right figure*), $850\,\mu\text{m}$ (*bottom-left figure*), $1380\,\mu\text{m}$ (*bottom-right figure*). The plots are for simulations with $b = 1.5$, which sets the detection limit (see Sect. 4.3).

are given in Table 2. Three different biases were used for the simulations ($b = 0, 0.75, 1.5$). Examples of maps at $500\,\mu\text{m}$ (Herschel) and $550\,\mu\text{m}$ (Planck) made with $b = 1.5$ and $b = 0$ are shown in Figs. 9 and 10. The difference in the spatial correlations is easily noticed in the Planck simulations. On the other hand, the smaller size of the Herschel simulations makes it more difficult to see the correlation.

The simulated maps and their associated catalogs are publicly available at <http://www.ias.u-psud.fr/irgalaxies/simulations.php>

4. Noise and source detection

The simulations can be used to test the detection capabilities of Planck/HFI and Herschel/SPIRE. For the first time these simulations use an empirical model that reproduces all the observational constraints from $5\,\mu\text{m}$ to $1.3\,\text{mm}$ and include the spatial correlation between the IR galaxies and the dark matter density field for galaxies up to very low luminosities ($L > 10^9 L_\odot$). They provide a useful tool for preparing future observations with Planck/HFI and Herschel/SPIRE.

4.1. Detection of bright sources

As stated previously bright sources dominate the power spectrum of the FIRB (see Fig. 3). We therefore need to subtract them

before studying the fluctuations in the background. In this section we concentrate on detecting them in three steps: 1) wavelet filtering, 2) detection, 3) measurement of the flux.

– Wavelet filtering: before trying to detect the sources we perform a wavelet transform of our simulated maps with the “atrou” algorithm. We remove spatial frequencies that are both higher and lower than the $FWHM$ of the PSF.

The small-scale filtering improves the estimation of the position of the sources when the instrumental noise is included in the simulations. In contrast to the confusion noise, the instrumental noise is not correlated for neighbouring pixels. This dominates errors in estimating the position of the sources.

The large-scale filtering corrects for a bias in the detection algorithm. The algorithm searches for sources using the absolute value of the pixel and not its value relative to its environment. This biases the detections towards sources in bright regions. The removal of the large spatial fluctuations corrects this effect.

The selection of spatial frequencies to be used for the detection has been manually optimised for each map to achieve a maximum number of reliable detections. This treatment is similar to what was done in the MIPS Spitzer maps (Dole et al. 2004). A comprehensive study of the application of the wavelet filtering technique for the source detections at long wavelengths for Planck and Herschel/SPIRE is beyond

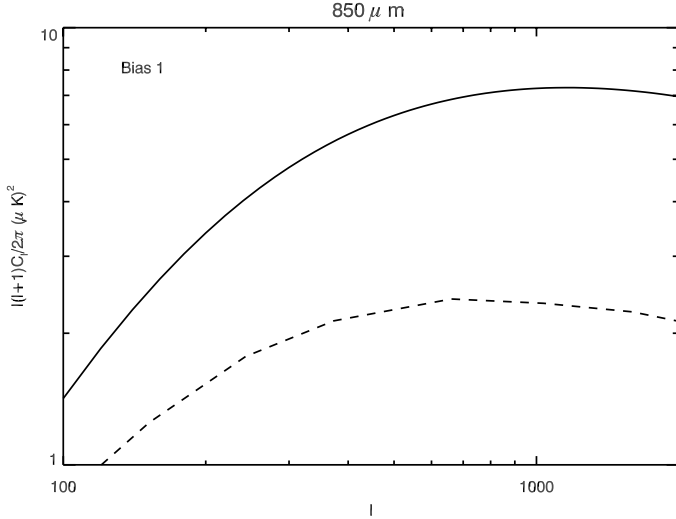


Fig. 8. Our power spectrum at $850 \mu\text{m}$ (continuous line) and that of Haiman & Knox (2000) (dashed line). The differences between both models arise from the differences in the emissivities (see Fig. 1). The lower level of the HK power spectrum comes from their lower emissivities. The emissivities of HK are at lower z and therefore favour larger angular scales for the power spectrum relative to our model.

Table 1. Physical size of the redshift slice $dz = 0.1$ (in Mpc) for different z .

z	1.0–1.1	2.0–2.1	3.0–3.1	4.0–4.1
$R_{dz=0.1}$ (Mpc)	233	139	93	67

Table 2. $FWHM$ of the PSF for different wavelengths of observation (in arc seconds) for all the simulated maps.

Wavelengths (μm)	350	550	850	1380	2097
Planck HFI $FWHM$ ('')	300	300	300	330	480
Wavelengths (μm)	250	350	550		
Herschel SPIRE $FWHM$ ('')	17	24	35		

the scope of this paper and has been fully discussed in e.g. López-Caniego et al. (2006).

- Detection algorithm: the algorithm is based on the “find” routine of the DAOPHOT library. In the filtered image the algorithm searches for peaks higher than a certain threshold σ_{thres} . It uses the PSF shape and the neighbouring pixels to analyse whether the peak is the centre of a source.
- Flux measurement: we developed a PSF fitting algorithm that we used in the original map (without filtering) to measure the flux of the sources. We decided whether the detections are real or false by two criteria: 1) proximity and 2) accuracy (see Sect. 4.1.1).

4.1.1. Bad detections

A detection is considered good or bad based on two criteria: 1) proximity with the position of an input source and 2) accuracy of flux for this source. The former requires that our detection is closer than $FWHM/5$ to at least one “neighbour” source in our catalog. The latter requires that the difference between the flux of one of the “neighbour” sources in the catalog and that of the detected source has to be smaller than the confusion and/or instrumental noise (see Tables 4 and 5). We consider the detection to be good only if both criteria are satisfied.

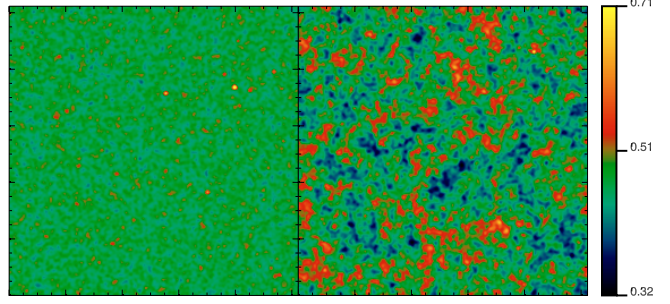


Fig. 9. Planck maps at $550 \mu\text{m}$ in MJy/sr with $b = 0$ (left) and $b = 1.5$ (right). The maps simulate a region of the sky of 49 square degrees with 1024 pixels of 25 arcsec.

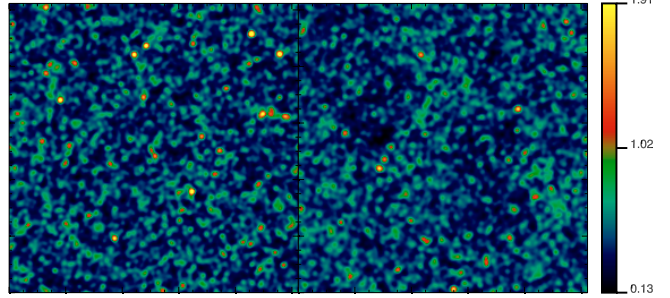


Fig. 10. Herschel maps at $500 \mu\text{m}$ in MJy/sr with $b = 0$ (left) and $b = 1.5$ (right). The maps simulate a region of the sky of 0.3 square degrees with 1024 pixels of 2 arcsec. The small size of the maps makes it difficult to appreciate the effect of the large-scale clustering.

The detection process also produces detections that do not comply with these criteria. We can see in Fig. 12 how the different σ_{thres} modify the rate of good-to-bad detections. For a low detection threshold ($\sigma_{\text{thres}} = 2\sigma_{\text{map}}$, i.e. for example 290 mJy/pix at Planck $350 \mu\text{m}$ for a map with $b = 0$ and no instrumental noise), the number of bad detections can become bigger than that of real detections. For a higher detection threshold ($\sigma_{\text{thres}} = 3\sigma_{\text{map}}$ i.e. 440 mJy/pix at $350 \mu\text{m}$), we find that the good detections dominate the bad ones, but we do not detect as many faint sources. Thus the number of false detections depends strongly on σ_{thres} . For different scientific goals, it can be interesting to use different σ_{thres} . For example, if we are interested in searching for objects at high redshifts, we could allow our detections to have 25% bad sources to be able to detect some interesting sources at high z . For studies of statistical properties of the sources, it would be necessary to use a stronger threshold. For our purpose, we used $\sigma_{\text{thres}} = 3\sigma_{\text{map}}$ ($\sim 10\%$ of false detections).

4.2. Instrumental and confusion noises

Instrumental and confusion noises have been studied both separately and in combination in order to quantify their relative contribution to the total noise. The estimated instrumental noises per beam for Planck and Herschel are given in Table 3. The instrumental noise per beam for Planck is the average one over the sky for a 1-year mission. The instrumental noise per beam for Herschel is typical of large surveys. We take the sensitivity of the so-called level 5 and level 6 of the Science Activity Group 1 (SAG 1) of the SPIRE guaranteed time team.

We studied the standard deviation of the measured fluxes in random positions for different maps. These maps were one of instrumental noise, three with different bias ($b = 0, 0.75, 1.5$)

Table 3. Simulation input instrumental noise per pixel of size equal to beam for Planck and for Herschel for a deep and a shallow survey.

Wavelengths HFI (μm)	350	550	850	1380	2097
$\sigma_{\text{Inst}}(\text{mJy})$	31.30	20.06	14.07	8.43	6.38
Wavelengths SPIRE (μm)	250	350	500		
σ_{Inst} Deep (mJy)	4.5	6.1	5.3		
σ_{Inst} Shallow (mJy)	7.8	10.5	9.2		

Table 4. Noise on the retrieved sources with only instrumental noise (σ_{I}), confusion noise (σ_{C}), and total noise ($\sigma_{\text{C+I}}$) in mJy for Planck/HFI.

Wavelengths HFI (μm)	350	550	850	1380	2097
σ_{I}	61.3	39.2	27.8	16.7	12.5
σ_{C} $b = 0$	111.5	41.5	14.7	4.6	2.1
σ_{C} $b = 0.75$	124	54.3	21.3	7.7	3.5
σ_{C} $b = 1.5$	158	79.8	30.4	10.9	5.4
$\sigma_{\text{C+I}}$ $b = 0$	126.7	62.3	33	17.4	13.2
$\sigma_{\text{C+I}}$ $b = 0.75$	153.6	75.3	38.4	19	13.8
$\sigma_{\text{C+I}}$ $b = 1.5$	188.2	95.3	46.7	21.1	14.4

Table 5. Instrumental noise (σ_{I}), confusion noise (σ_{C}) and total noise ($\sigma_{\text{C+I}}$) in mJy for Herschel/SPIRE.

Wavelengths SPIRE (μm)	250	350	500
Deep σ_{I}	8.7	11.3	10.1
Shallow σ_{I}	15	20.1	18.2
σ_{C} $b = 0, 0.75, 1.5$	4.6	6.5	5.5
Deep $\sigma_{\text{C+I}}$	9.8	12.3	11
Shallow $\sigma_{\text{C+I}}$	16	20.8	19

but without instrumental noise, and complete maps created by adding the map of instrumental noise to the three source maps. We call these maps hereafter instrumental-only, confusion-only, and complete-maps. We fit a Gaussian to the histogram of the fluxes measured in these random positions and considered the standard deviation of this Gaussian as the best estimate of the standard deviation of the photometry of a source and therefore of the 1σ instrumental, confusion, and total noise. Results are shown in Tables 4 and 5.

The confusion noise increases with the bias. This effect is noticeable for the Planck observations, but not for the Herschel ones because of the higher Herschel/SPIRE angular resolution. Also, for the considered Herschel/SPIRE surveys, the instrumental noise is always greater than the confusion noise. For Planck the correlation effect is more noticeable for longer wavelengths since they probe progressively higher redshifts and therefore higher dark-matter power spectra, as discussed in Sect. 2.3 (see Fig. 5).

The total noise $\sigma_{\text{C+I}}$ is close to the value $\sigma_{\text{C+I}}^2 = \sigma_{\text{C}}^2 + \sigma_{\text{I}}^2$ (see Tables 4 and 5). For Planck at short wavelengths ($350\,\mu\text{m}$ and $550\,\mu\text{m}$), the confusion noise is the dominant source of noise. The instrumental noise becomes dominant at $850\,\mu\text{m}$ for $b = 0$ and $b = 0.75$. For longer wavelengths, it dominates for any bias. For Herschel the instrumental noise dominates the total noise for both the shallow and deep surveys. The confusion noise is not strongly affected by the bias because of the small $FWHM$ of the PSF.

4.3. Completeness

The first study of the point-sources detection limit for Planck was carried out based on a generalisation of the Wiener

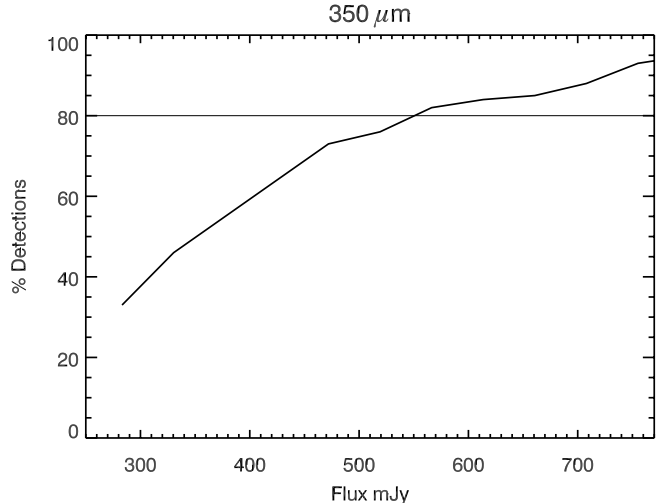


Fig. 11. Study of completeness for Planck/HFI with $b = 0$ at $350\,\mu\text{m}$. The horizontal straight line marks 80% of completeness.

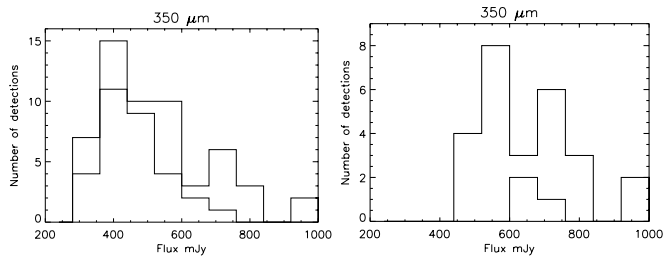


Fig. 12. Good detections (thick line) vs. bad detections (thin line) *Left:* histogram of good and bad detections using small σ_{thres} (290 mJy). *Right:* histogram of good and bad detections using higher σ_{thres} (440 mJy) in the same map. Both plots have been done using a Planck simulated map with $b = 0$.

filtering method (Bouchet & Gispert 1999). Recently López-Caniego et al. (2006) used the most recent available templates of the microwave sky and extragalactic point source simulations, including both the radio and IR galaxies, to estimate the Planck detection limits. Here we revisit those results with new models for IR galaxies and the last noise estimates for Planck/HFI and Herschel/SPIRE.

For the study of the completeness, a number N_A of sources of equal flux are randomly distributed in the maps. Each source is placed far enough from the other to avoid these additional sources contributing to the confusion noise. The detection and photometry of these sources is carried out as described at the beginning of the section. We call N_G the number of good detections that comply with the “proximity” and “accuracy” criteria. The completeness for this flux C_F is then calculated as $C_F = \frac{N_G}{N_A} \times 100$. The completeness of the detections of sources for a given flux depends on both the instrumental noise and the confusion noises. The results for the completeness are averaged over ~ 3000 individual fake sources per flux. An example of the completeness at $350\,\mu\text{m}$ is shown in Fig. 11. Results for all wavelengths are given in Tables 6 and 7. They are consistent with the instrumental, confusion, and total noises given in Sect. 4.2 and the conclusions from that section remain valid for the completeness. For simulated maps including both extragalactic sources and instrumental noise, we find that the 80% completeness level coincide with flux limits around 4–5 σ .

Table 6. Completeness limits (in mJy) for the Planck/HFI maps with instrumental noise (C_I), confusion noise (C_C) and both (C_{C+I}). We consider $b = 0, 0.75$, and 1.5 .

Wavelengths HFI (μm)	350	550	850	1380	2097
$C_I = 80\%$	236	157	108	67	50
$C_C = 80\% b = 0$	516	174	60.5	20	8.6
$C_C = 80\% b = 0.75$	550	239.5	88.5	30.5	15.5
$C_C = 80\% b = 1.5$	684	300	121	40	24
$C_{C+I} = 80\% b = 0$	560	234	126	71	52
$C_{C+I} = 80\% b = 0.75$	607	290	141	74	55
$C_{C+I} = 80\% b = 1.5$	709	360	171	80	58.5

Table 7. Completeness limits (in mJy) for the Herschel/SPIRE maps with instrumental noise (C_I), confusion noise (C_C), and both (C_{C+I}).

Wavelengths SPIRE (μm)	250	350	500
Deep $C_I = 80\%$	33	45.9	37.9
Shallow $C_I = 80\%$	57.3	84.2	67.3
$C_C = 80\%$	35	32	27.4
Deep $C_{C+I} = 80\%$	49.8	64.4	48.4
Shallow $C_{C+I} = 80\%$	70	96.5	75.5

Taking these 80% completeness limits as a detection threshold, the prediction for the number of sources detected directly by Herschel/SPIRE for the deeper survey considered here is $8.3 \times 10^5/\text{sr}$ at $250 \mu\text{m}$, $1.1 \times 10^5/\text{sr}$ at $350 \mu\text{m}$, and $1.8 \times 10^4/\text{sr}$ at $500 \mu\text{m}$. The fraction of resolved CFIRB varies between 8 and 0.3% from 250 to $500 \mu\text{m}$.

5. CIB fluctuations

The Planck and Herschel/SPIRE surveys allow an unprecedented search for CFIRB fluctuations associated with large-scale structure and galaxy clustering. Background fluctuations probe the physics of galaxy clustering over an ensemble of sources, with the bulk of the signal contribution originating from sources well below the detection threshold. Thus a comprehensive fluctuation analysis is an essential complement to the study of individually detected galaxies. In this section, we restrict ourselves to predictions for Planck/HFI, excluding the 143 and 100 GHz channels. At these low frequencies, we are dominated by the non-thermal emission of the radiosources – that are not including in our model – and the Poisson term dominates the clustering term (e.g. González-Nuevo et al. 2005). Also, we exclude the Herschel/SPIRE case since our simulations include the clustering of CIB sources in two different halos (2h), but not the clustering within the same halo (1h). The 1h term dominates for $\ell \gtrsim 3000$ and will be accurately measured by Herschel/SPIRE. Only large-scale surveys can put strong constraints on the 2h term. Measuring the 2h clustering with CFIRB anisotropies is one of the goals of Planck/HFI.

5.1. Contributors to the angular power spectrum

From the far-IR to the millimeter, the sky is made up of the CFIRB and two other sources of signal, the galactic cirrus and the CMB (we neglect the SZ signal). Understanding our observations of the CFIRB requires understanding the contributions from these two components which act for us as foreground and background contamination.

The galactic cirrus acts as foreground noise for the CFIRB. The non-white and non-Gaussian statistical properties of its emission make it a very complex foreground component. The

power spectrum of the IRAS $100 \mu\text{m}$ emission is characterised by a power law Gautier et al. (e.g. 1992). Here we compute the angular power spectrum of the dust emission following Miville-Deschénes et al. (2007). These authors analysed the statistical properties of the cirrus emission at $100 \mu\text{m}$ using the IRAS/IRIS data. We used their power spectrum normalization and slope (varying with the mean dust intensity at $100 \mu\text{m}$). Using the average $|b| > 30^\circ$ spectrum of the HI-correlated dust emission measured using FIRAS data, we converted the $100 \mu\text{m}$ power spectra to the Planck wavelengths. For the discussion, we considered both the total cirrus fluctuations and 10% residual fluctuations. These 10% could be achievable with Planck in low dust-column-density regions containing ancillary HI data.

The CMB acts as background noise for the CFIRB. However, the CMB angular power spectrum is known to an accuracy of 1% or better (Planck-HFI web site: <http://www.planck.fr/>). This combines with its well-known spectral dependence to allow for a clean subtraction of its contribution that in turn allows for detections of the CFIRB C_I even for wavelengths where the CMB dominates. We consider for the rest of the discussion a conservative assumption, that is that the residual CMB fluctuations are approximately 2%.

The angular power spectrum of IR galaxies is composed of a correlated and a Poissonian part. As discussed in Sect. 2.1, the contribution to the Poissonian part is dominated by relatively faint sources after subtracting the brightest galaxies (see Fig. 3). We consider that we can remove sources brighter than our 80% completeness detection limit (see Tables 6 and 7). For doing so, we use the technique described in Sect. 4.1 for measuring the position and fluxes of the sources and once these are known we subtract a PSF with the measured flux from the map.

The correlated C_I is obtained as described in Sect. 2.1. For the relative error on the power spectrum, we follow Knox (1995):

$$\frac{\delta C_I}{C_I} = \left(\frac{4\pi}{A} \right)^{0.5} \left(\frac{2}{2l+1} \right)^{0.5} \left(1 + \frac{A\sigma_{\text{pix}}^2}{NC_I W_l} \right)$$

where A is the observed area, σ_{pix} the rms noise per pixel (instrumental plus confusion), N the number of pixels, and W_l the window function for a map made with a Gaussian beam $W_l = e^{-l^2\sigma_b^2}$.

5.2. Detectability of CFIRB correlated anisotropies

The study of the C_I on different scales allows us to study different aspects of the physics of the environment of IR galaxies (see Cooray & Sheth 2002). Large scales ($l < 100$) give information on the cosmological evolution of primordial density fluctuations in the linear phase and therefore on the cosmological parameters. Intermediate scales are mostly influenced by the mass of dark halos hosting sources, which determines the bias parameter. Small scales ($l > 3000$) probe the distribution of sources in the dark-matter halos and therefore the non-linear evolution of the structures. This non linear evolution was not accounted for in our model.

We can see in Fig. 13 the different contributions to the C_I for Planck/HFI: the correlated CFIRB C_I with $b = 1$ and $b = 3$ with their respective error bars ($\Delta\ell/\ell = 0.5$), Poissonian fluctuations, dust, and CMB contributions. The dust and CMB C_I are plotted both before and after implementing the corrections discussed above (10% and 2% residuals, respectively). For the dust we selected for the estimation of the column density a field centred on the SWIRE/ELAIS S1 field. This field has a very low level of dust contamination. For a 400 sq. deg. area centred at $(l, b) = (311^\circ, -73^\circ)$, we have an average HI column

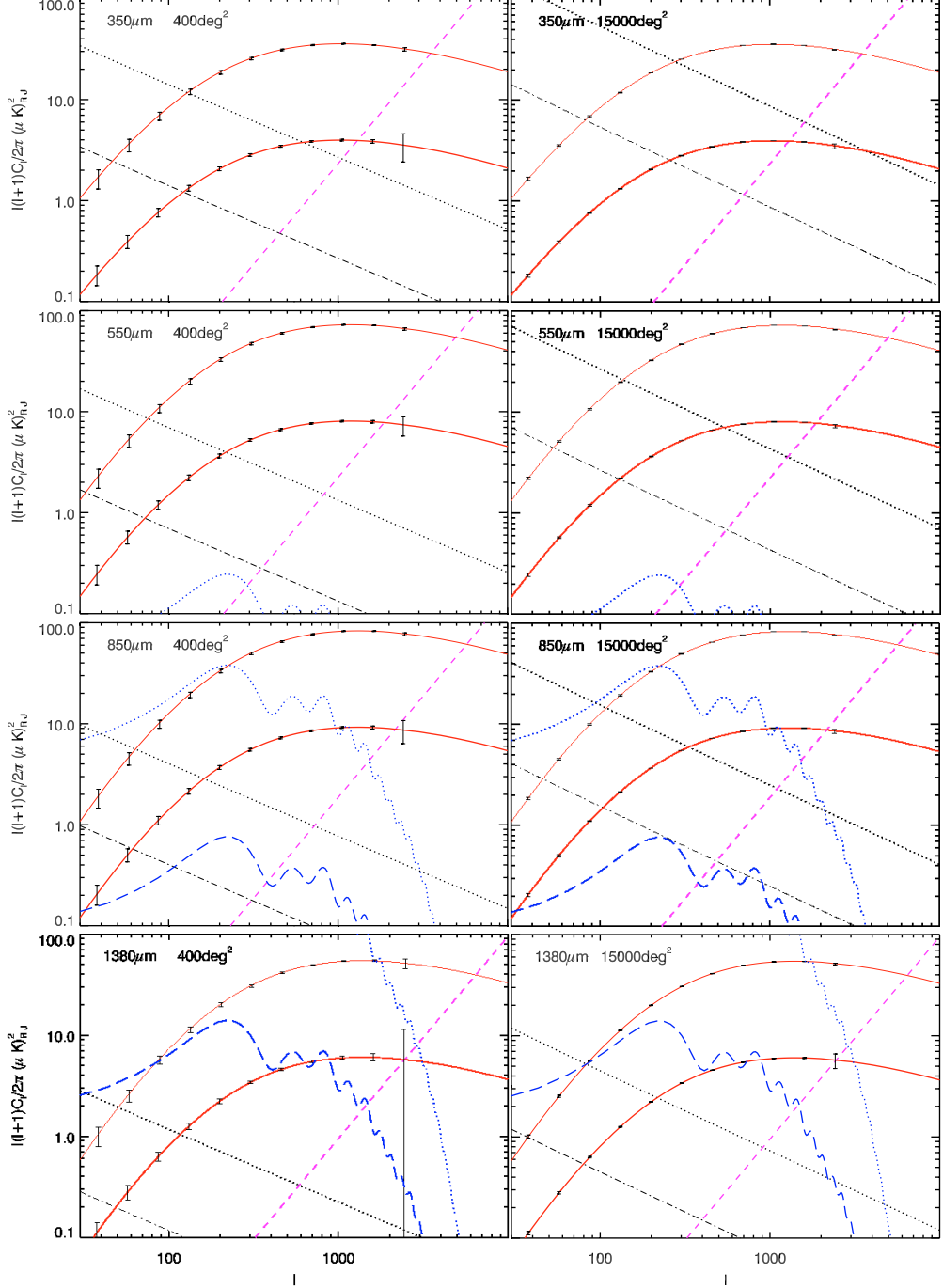


Fig. 13. Power spectra for Planck of the correlated IR galaxies with $b = 1$ (thick continuous line) and $b = 3$ (thin continuous line), Poisson fluctuations for sources fainter than 709, 363, 171, 80 mJy at 350, 550, 850 and 1380 μm respectively (short dashed line), dust with an HI column density of 1.5×10^{20} at/cm 2 and 2.7×10^{20} at/cm 2 for the 400 Sq. Deg. and ~ 15000 Sq. Deg. considered regions respectively (dotted line), dust/10 (dotted-dashed line), CMB (dotted line) and CMB/50 (dashed line). Error bars are computed using $\Delta\ell/\ell = 0.5$.

density of only 1.5×10^{20} at/cm 2 . We also take the whole sky above $|b| > 40^\circ$ (~ 150000). The average HI column density is 2.7×10^{20} at/cm 2 .

At all wavelengths, the correlated CFIRB C_1 is dominated by the other components on both very large and very small scales. The angular frequencies where the C_1 is dominated by the galaxy correlation depends mainly on the wavelength, if the bias and cirrus level are fixed. On large scales the C_1^{CFIRB} is dominated by the dust for wavelengths up to 550 μm , and for longer wavelengths it is dominated by the CMB. On small scales the Poissonian fluctuations dominate the power spectra.

We can see in Tables 8 and 9 the ranges for which CFIRB-correlated anisotropies are dominating depending on whether we consider a partial subtraction of the cirrus and CMB or not. On small angular scales (large ℓ), the range of ℓ where the correlated C_1 dominates increases with the wavelength. On large angular scales (small ℓ), the results depend on whether we consider partial subtraction of the cirrus and CMB or not.

Table 8 shows the ℓ ranges for where CFIRB correlated anisotropies are dominating when no subtraction of the dust or CMB has been performed. At large angular scales and wavelengths up to 850 μm the detectability is better for the small map

Table 8. Multipole ℓ ranges where the CFIRB correlated anisotropies are higher than the cirrus and CMB components.

Wavelengths (μm)	350	550	850	1380
400 Sq. Deg. $b = 1$	$600 < \ell < 1200$	$200 < \ell < 1800$	$1000 < \ell < 2200$	Indetectable
400 Sq. Deg. $b = 3$	$120 < \ell < 3500$	$75 < \ell < 5000$	$240 < \ell < 6000$	$1800 < \ell < 6500$
15 000 Sq. Deg. $b = 1$	Indetectable	$550 < \ell < 1800$	$1200 < \ell < 2200$	Indetectable
15 000 Sq. Deg. $b = 3$	$280 < \ell < 3500$	$130 < \ell < 5000$	$230 < \ell < 6000$	$1800 < \ell < 6500$

Table 9. Multipole ℓ ranges where the CFIRB correlated anisotropies are higher than the residual cirrus and CMB components (10%, and 2% respectively).

Wavelengths (μm)	350	550	850	1380
400 Sq. Deg. $b = 1$	$200 < \ell < 1200$	$80 < \ell < 2100$	$60 < \ell < 2200$	Indetectable
400 Sq. Deg. $b = 3$	$40 < \ell < 3500$	$30 < \ell < 5000$	$25 < \ell < 6000$	$80 < \ell < 6500$
15 000 Sq. Deg. $b = 1$	$250 < \ell < 1200$	$130 < \ell < 1800$	$100 < \ell < 2200$	Indetectable
15 000 Sq. Deg. $b = 3$	$80 < \ell < 3500$	$55 < \ell < 5000$	$45 < \ell < 6000$	$80 < \ell < 6500$

because of its lower $N(\text{HI})$ column density. Without any dust contamination correction, this prevents us from taking advantage from the smaller error on the estimation of the C_1 in the very large area surveys and makes both kind of observation complementary. In clean regions of the sky, the best wavelengths for the observation of the large scales CFIRB anisotropies are $350 \mu\text{m}$ and $550 \mu\text{m}$.

The large-scale detectability drastically improves in the case of partial subtraction of the CMB and dust cirrus as seen in Table 9. As discussed above we expect to be able to subtract the dust fluctuations and the CMB to a 10% and 2% of their original level. This does not change our ability to measure the correlated CFIRB C_1 on small scales (due to the high confusion noise), but will allow us to probe larger scales.

6. Summary

This paper presented new simulations of the cosmic infrared and submillimeter background. The simulations are based on an empirical model of IR galaxy evolution (the LDP model) combined with a simple description of the correlation. The IR galaxy spatial distribution follows that of the dark-matter halo density field, with a bias parameter accounting for the possibility of the luminous matter being more or less correlated with the dark matter. The simulated maps and their catalogs are publicly available at <http://www.ias.u-psud.fr/irgalaxies/simulations.php>. Other maps are available upon request. These maps are intended to be a useful tool for planning future large IR and submillimeter surveys. In this paper, we used the maps to predict the confusion noise and completeness levels for Planck/HFI and Herschel/SPIRE. We also predicted the power spectra of correlated CFIRB anisotropies for Planck/HFI which will be a major advance in the study of the CFIRB anisotropies at large scales (i.e. $\ell < 2000\text{--}5000$ depending on the wavelengths). Further analysis of the CFIRB anisotropies, including the use of stacking analysis to isolate the anisotropies in different redshift ranges, will be presented in a second paper, now in preparation.

References

- Adelberger, K. L., Steidel, C. C., Giavalisco, M., et al. 1998, ApJ, 505, 18
 Bardeen, J. M., Bond, J. R., Kaiser, N., & Szalay, A. S. 1986, ApJ, 304, 15

- Bertoldi, F., Menten, K. M., Kreysa, E., Carilli, C. L., & Owen, F. 2000, ArXiv Astrophysics e-prints
 Blain, A. W., Chapman, S. C., Smail, I., & Ivison, R. 2004, ApJ, 611, 725
 Bouchet, F. R., & Gispert, R. 1999, New Astron., 4, 443
 Brand, K., Rawlings, S., Hill, G. J., & Lacy, M. 2003, New Astron. Rev., 47, 325
 Cooray, A., & Sheth, R. 2002, Phys. Rep., 372, 1
 Dole, H., Gispert, R., Lagache, G., et al. 2001, A&A, 372, 364
 Dole, H., Lagache, G., & Puget, J.-L. 2003, ApJ, 585, 617
 Dole, H., Le Floc'h, E., Pérez-González, P. G., et al. 2004, ApJS, 154, 87
 Dole, H., Lagache, G., Puget, J.-L., et al. 2006, A&A, 451, 417
 Dye, S., Eales, S. A., Ashby, M. L. N., et al. 2006, ApJ, 644, 769
 Elbaz, D., Cesarsky, C. J., Chanial, P., et al. 2002, A&A, 384, 848
 Elbaz, D. 2005, Space Sci. Rev., 119, 93
 Farrah, D., Lonsdale, C. J., Borys, C., et al. 2006, ApJ, 641, L17
 Fixsen, D. J., Dwek, E., Mather, J. C., Bennett, C. L., & Shafer, R. A. 1998, ApJ, 508, 123
 Gautier, III, T. N., Boulanger, F., Perault, M., & Puget, J. L. 1992, AJ, 103, 1313
 Genzel, R., & Cesarsky, C. J. 2000, ARA&A, 38, 761
 Giavalisco, M., Steidel, C. C., Adelberger, K. L., et al. 1998, ApJ, 503, 543
 González-Nuevo, J., Toffolatti, L., & Argüeso, F. 2005, ApJ, 621, 1
 Grossan, B., & Smoot, G. F. 2007, A&A, 474, 731
 Haiman, Z., & Knox, L. 2000, ApJ, 530, 124
 Hauser, M. G., Arendt, R. G., Kelsall, T., et al. 1998, ApJ, 508, 25
 Holland, W. S., Cunningham, C. R., Gear, W. K., et al. 1998, ArXiv Astrophysics e-prints
 Knox, L., Cooray, A., Eisenstein, D., & Haiman, Z. 2001, ApJ, 550, 7
 Knox, L. 1995, Phys. Rev. D, 52, 4307
 Lagache, G., & Puget, J. L. 2000, A&A, 355, 17
 Lagache, G., Dole, H., & Puget, J.-L. 2003, MNRAS, 338, 555
 Lagache, G., Dole, H., Puget, J.-L., et al. 2004, ApJS, 154, 112
 Lagache, G., Puget, J.-L., & Dole, H. 2005, ARA&A, 43, 727
 Lagache, G., Bavouzet, N., Fernandez-Conde, N., et al. 2007, ApJ, 665, L89
 Lahav, O., & Suto, Y. 2004, Liv. Rev. Relativ., 7, 8
 López-Caniego, M., Herranz, D., González-Nuevo, J., et al. 2006, MNRAS, 370, 2047
 Magliocchetti, M., Silva, L., Lapi, A., et al. 2007, MNRAS, 375, 1121
 Marinoni, C., Le Fevre, O., Meneux, B., & the VVDS team 2006, ArXiv Astrophysics e-prints
 Matsuhara, H., Kawara, K., Sato, Y., et al. 2000, A&A, 361, 407
 Miville-Deschénes, M.-A., Abergel, A., & Boulanger, F. 2001, Dust Evolution in the Cold and Diffuse Interstellar Medium: The Herschel Perspective, The Promise of the Herschel Space Observatory, ed. G. L. Pilbratt, J. Cernicharo, A. M. Heras, T. Prusti, & R. Harris, ESA SP-460, 471
 Miville-Deschénes, M., Lagache, G., Boulanger, F., & Puget, J. 2007, ArXiv e-prints, 704
 Negrello, M., Perrotta, F., Gonzalez-Nuevo Gonzalez, J., et al. 2007, ArXiv Astrophysics e-prints
 Papovich, C., Dole, H., Egami, E., et al. 2004, ApJS, 154, 70
 Puget, J.-L., Abergel, A., Bernard, J.-P., et al. 1996, A&A, 308, L5
 Saunders, W., Rowan-Robinson, M., & Lawrence, A. 1992, MNRAS, 258, 134
 Steidel, C. C., Adelberger, K. L., Dickinson, M., Giavalisco, M., & Pettini, M. 1998, ArXiv Astrophysics e-prints
 Wang, W.-H., Cowie, L. L., & Barger, A. J. 2006, ApJ, 647, 74